

Undistorted Lensed Images in Galaxy Clusters

L. L. R. Williams^{1*} and G. F. Lewis^{1,2†}

¹*Institute of Astronomy, Madingley Road, Cambridge, CB3 0HA, U.K.*

²*Astronomy Group, Dept. of Earth and Space Sciences, SUNY at Stony Brook, NY 11794-2100, U.S.A.*

Accepted to MNRAS

ABSTRACT

To date, the study of high-magnification gravitational lensing effects of galaxy clusters has focused upon the grossly distorted, luminous arc-like features formed in massive, centrally condensed clusters. We investigate the formation of a different type of image, highly magnified yet undistorted, in two widely employed cluster mass density profiles; an isothermal sphere with a core, and a universal dark matter halo profile derived from numerical simulations of Navarro et al. We examine the properties of images of extended sources produced by these two clusters profiles, paying particular attention to the undistorted images. Using simple assumptions about the source and lens population, we estimate the relative frequency of occurrence of highly magnified, undistorted images and the more commonly known giant arcs.

Key words: Gravitational Lensing, Clusters of Galaxies

1 INTRODUCTION AND MOTIVATION

Gravitational lensing by rich galaxy clusters produces highly magnified, grossly distorted images of background galaxies (Fort & Mellier 1994, Schindler et al. 1995, Lavery 1996). The mechanism of production of these “giant arcs” is well understood; in fact, the observed arcs are commonly used to determine the mass distribution in the lensing clusters (Lavery & Henry 1988, Fort & Mellier 1994, Kneib et al. 1995). Despite their low surface brightness, the giant arcs are highly visible and easily detected due to their unique morphology.

However, it is possible that galaxy clusters are capable of producing highly magnified yet *undistorted* images of background sources. Whether such images are produced in reasonable numbers depends on the cluster mass profiles: steep density gradients produce thin arc-like images (Hammer 1991, Wu & Hammer 1993), whereas flat central cores can easily give rise to undistorted images. Because of their regular morphology these latter images would not be as prominent as arcs, and so would not be readily recognized and studied.

Undistorted magnified images are the subject of the present paper. Our aim is two-fold. First, we ask whether realistic cluster profiles can produce highly magnified undistorted images, or HMUs, and if so, under what conditions. We consider two types of clusters: an isothermal model with a core, and a universal dark matter cluster model derived

from the numerical simulations of Navarro, Frenk, & White (1995, 1996). The major difference between these two profiles occurs in their central regions: isothermal models have a flat density core, whereas those drawn from numerical simulations are characterized by gradually flattening logarithmic slope, with decreasing radius, and are singular at the centre. We examine the image properties produced by these two profiles, paying particular attention to HMUs. Second, we use simple assumptions about cluster and source properties to estimate how common such HMU images might be. As a way to avoid some parameter dependencies, we do not calculate the actual frequency of occurrence of such images, instead we estimate the *ratio* of the frequency of HMUs to giant arcs for the two different cluster mass profiles. In the present paper we calculate this ratio assuming circularly symmetric clusters, whereas real clusters exhibit substructure which can greatly increase the clusters’ cross-section for generating arcs (Bartelmann et al. 1995). However our results can be readily converted to apply to substructured clusters, as outlined in the Conclusions.

Our results indicate that the statistics of HMUs are quite dependent on the overall form of the lensing potential, suggesting a diagnostic tool of cluster cores. Such a probe of clusters centres is welcome as current observational techniques have yet to resolve the matter distribution in the inner regions of clusters. Dynamical methods are generally inadequate in addressing the issue because of their reliance on assumptions (cluster is relaxed, mass follows light), as well as the small numbers of galaxy radial velocities (eg. Sadat 1997). X-ray methods are more promising because the emitting gas is in hydrostatic equilibrium with the cluster

* Email: llrw@ast.cam.ac.uk

† Email: gfl@brenda.ess.sunysb.edu

gravitational potential. X-ray derived cores tend to be large; based on the whole sample of the EMSS clusters, Henry et al. (1992) estimate that the average cluster core radius is $125h^{-1}$ kpc. These results are in apparent contradiction with strong lensing analysis of clusters. Le Fèvre et al. (1994), based on a sample of 16 brightest high- z EMSS clusters, conclude that arc statistics are incompatible with X-ray core radii, and much smaller cores are required. However, Waxman & Miralda-Escudé (1995), and Miralda-Escudé & Babul (1995) pointed out that X-ray and lensing observations can be reconciled, and both are compatible with a singular dark matter potential like the universal dark matter profile, since multi-phase cooling flow gas in this type of a potential tends to be isothermal, and naturally produces cores. In any case, X-ray observations do not constrain cluster dark matter cores. That leaves us with lensing. Lensing is favored among other techniques because it directly probes the distribution of all mass regardless of its baryonic/non-baryonic nature, dynamical and physical state. Strong lensing observations place a tight upper limit on cluster cores; however it is possible that lensing clusters with giant arcs are a biased sample of clusters, because steeper-than-average density profiles are more likely to produce thin long arcs. Consequently, cores of $\sim 50h^{-1}$ kpc, or even larger, may still prove to be a common feature of clusters. In fact, there is tentative observational evidence for the existence of cluster cores: (i) Cl0024+1654 is a spectacular cluster-lens with five HST-resolved images of a high- z galaxy. The presence of the central demagnified image E requires the cluster to have a finite core (Colley et al. 1996, Smail et al. 1996); (ii) An extended highly luminous $z = 2.7$ galaxy was recently discovered $6''$ from the center of an intervening cluster (Yee et al. 1996). Even though its true ‘lensing status’ is still uncertain, its properties can be explained if the lensing cluster had a core (Williams & Lewis 1996, but see Seitz et al. 1997). Thus the existence and sizes of flat cluster cores is still a matter of debate.

If found, HMU images themselves would prove useful for the detailed study of galaxies at high redshift. Many highly distorted arcs have already been studied to deduce the properties of the high- z sources. For example, their star formation rate can be derived because spectra of magnified sources can be obtained with a reasonable telescope integration time (Ebbels et al. 1997). High-resolution HST observations of lensed galaxies are used to infer galaxy morphologies (Smail et al. 1996). However, the distorted appearance of arcs, coupled with the complicated nature of the lens model, implies that lensing inversions, which are needed in order to derive the kinematic and structural properties of the source galaxy, are difficult. Ideally, one would like to observe the overall simpler case of highly magnified undistorted images.

2 CLUSTER MASS PROFILE MODELS

We consider two circularly symmetric cluster mass profiles: isothermal sphere with a core (ISC) and the Navarro et al. (1996) universal dark matter profile (NFW).

The 2D projected mass density profile of ISC model is given by

$$\Sigma(r) = \Sigma_0 \frac{1 + p(r/r_c)^2}{[1 + (r/r_c)^2]^{2-p}}. \quad (1)$$

We adopt $p = 0.5$ to obtain an isothermal sphere at large radii; the ISC model. However any value between 0 and 0.5 results in a realistic mass model; a $p = 0$ represents a Plummer model [see Schneider et al. (1992) a detailed description of the profile]. In Equation 1, r_c is the core radius, and Σ_0 is the central surface mass density.

The 3D mass density profile of the NFW model is,

$$\rho(r) = \frac{\rho_s r_s}{r(1 + r/r_s)^2}, \quad (2)$$

where r_s is the scale radius, and ρ_s is the mass density at $r \approx 0.466 r_s$. This model is derived from N-body simulations of large scale structure and is found to be applicable on scales of $3 \times 10^{11} \lesssim M_{200}/M_\odot \lesssim 3 \times 10^{15}$, where M_{200} is the mass within a radius r_{200} . Within this radius the mean overdensity is a factor of 200.

We use normalised lengths, $x = r/r_c$ and $x = r/r_s$, respectively, and express the surface mass density in terms of the critical surface density for lensing,

$$\kappa(x) = \frac{\Sigma(x)}{\Sigma_{crit}}, \quad \Sigma_{crit} = \frac{c^2}{4\pi G} \frac{D_{os}}{D_{ol}D_{ls}}, \quad (3)$$

where D_{ij} are the relative angular diameter distances between the observer (o), lens (l) and source (s).

For ISC model, the normalized surface mass density is

$$\kappa(x) = \kappa_0 \frac{1 + px^2}{[1 + x^2]^{2-p}}. \quad (4)$$

For NFW model, the corresponding equation was calculated by Bartelmann (1996), who showed that NFW model is compatible with the existence of radial arcs in clusters. We reproduce the relevant equations here for completeness;

$$\kappa(x) = 2\kappa_s \frac{f(x)}{x^2 - 1}, \quad \text{where } \kappa_s = \rho_s r_s / \Sigma_{crit}, \quad (5)$$

$$\text{and } f(x) = \begin{cases} 1 - \frac{2}{\sqrt{x^2 - 1}} \arctan \sqrt{\frac{x-1}{x+1}} & (x > 1) \\ 1 - \frac{2}{\sqrt{1-x^2}} \operatorname{arctanh} \sqrt{\frac{1-x}{1+x}} & (x < 1) \\ 0 & (x = 1) \end{cases} \quad (6)$$

For a circularly symmetric lens, the lens equation, which is the relation between the source position y , the image position x , and the deflection angle, is given by

$$y = x - \frac{\int_0^x 2x' \kappa(x') dx'}{x} = x - \frac{m(x)}{x}, \quad (7)$$

where $m(x)$ is the dimensionless mass interior to x , in units of $(c^2/4G)(D_{os}D_{ol}/D_{ls})$.

A lensed image is distorted both radially and tangentially with respect to the centre of the lensing potential. The tangential distortion is the ratio of the tangential size of the image to that of the source; for a sufficiently small source it is given by the ratio of their respective distances from lens centre, x/y . Similarly, the radial distortion is dx/dy , if the source’s radial extent is dy . Since magnification is just the ratio of the size of the image to that of the source, it is given by

$$\mu = \left| \frac{dx}{dy} \frac{x}{y} \right|. \quad (8)$$

The length-to-width ratio of an image whose source is circular is,

$$L/W = \left| \frac{dy}{dx} \frac{x}{y} \right|, \quad (9)$$

and is the most commonly used measure of image distortion. Note that an isothermal density profile, $\kappa(x) \propto x^{-1}$, implies that $dy/dx = 1$ (Equation 7), i.e. images suffer no radial (de)magnification. Steeper profiles always result in radially demagnified images, while shallower profiles usually produce radially magnified images.

Using Equations 4-9 we can calculate all the image properties needed in this paper.

3 IMAGE PROPERTIES

3.1 ISC model

The top panel of Figure 1 shows the relation between the image and source positions, for two values of κ_0 , of an ISC model. Supercritical clusters, represented here by $\kappa_0 = 1.1$ case (solid lines), produce three images if the source impact parameter is smaller than the radial caustic, y_r [see Eqn (8.42) of Schneider et al. (1992)]. Subcritical clusters, such as $\kappa_0 = 0.9$ case (dashed line) always produce one image, and the x - y relation is one-to-one and monotonically increasing.

Figure 2 shows the relation between image magnification and distortion. Two supercritical cases are shown: solid lines are the three images of a $\kappa_0=3.0$ lens, and dot-dash lines are for a $\kappa_0=1.1$ lens. The long-dash line is the single image of a critical lens, $\kappa_0=1.0$, while the short-dash line is the single image of a $\kappa_0=0.9$ lens. Each lens with $\kappa_0 > 1$ has three branches corresponding to three images. The primary image, which is formed at the minimum of the lensing potential [see Schneider (1985) and Blandford & Narayan (1986)], is labeled I. This image appears on the same side of the lens centre as the unlensed source, and is tangentially extended into an arc, with $L/W > 1$. It is always magnified with respect to the source. The image formed at the saddle-point of the lensing potential, sometimes called the ‘counter arc’, possesses reversed parity and is labeled II. The central image, labeled III, is formed at the maximum of the lensing potential, and is radially extended, i.e. has $L/W < 1$. Images II and III are on the side of the lens opposite to the location of the source. Note that for very centrally condensed lenses, i.e. those with $\kappa_0 > 2$, image III can be demagnified, $\mu < 1$, if the source is sufficiently close to the lens centre.

The ‘hidden’ parameter in this plot is the source position, y . To illustrate its influence on the location of the images, we have plotted the three images of a source at $y = 0.010$ (empty circles), and the three images of a source at $y = 0.016$ (solid dots), for a $\kappa_0=1.1$ lens. As the source approaches the lens centre in projection, images I and II get very elongated and tend to merge along the tangential critical line; while image III moves close towards the lens centre.

Notice that the single image branch of a $\kappa_0 < 1$ lens joins to and continues as the branch of the central image, labeled III, of the corresponding $2 - \kappa_0$ lens. As an example, the image of a $\kappa_0 = 0.9$ lens (short-dash line) continues as the central image branch of a $\kappa_0 = 1.1$ lens. This can be shown as follows. For image position x very close to the lens centre image magnification, $\mu \approx (1 - \kappa_0)^{-2}$, has the same numerical value for a κ_0 as well as a $2 - \kappa_0$ lens. The distortion

L/W of the image located at the centre is 1, from symmetry. Therefore, for small x , the branches of central images of a κ_0 and a $2 - \kappa_0$ lens meet at the same point in the $\log(L/W)$ vs. $\log(\mu)$ diagram. The slope of both the branches at this point can be shown to be $d \log(L/W)/d \log(\mu) = -\frac{1}{2}$, independent of κ_0 , and p ; therefore these two branches are continuous.

The most visible feature in a lensing cluster is the primary arc, since it is always well displaced from the cluster centre, is highly elongated and always magnified. For this image, the magnification is an increasing function of distortion. This is why high magnification is associated with high distortion of lensed images in galaxy clusters. However high magnification need not always imply high distortion.

It is apparent from Figure 2 that subcritical clusters, represented here by a $\kappa_0 = 0.9$ case, can produce highly magnified undistorted images[‡]. For example, if the source is located close to the centre of a $\kappa_0 = 0.9$ lens, its magnification is ~ 100 , while its distortion is negligible. In fact, the largest L/W ratio attained by an image of any subcritical lens is not greater than $L/W = 3$, as we now show.

The length-to-width ratio of any image in the ISC cluster model can be derived from Equations 9, 7, and 4;

$$L/W = \frac{1 - \kappa_0(1 + x^2)^{p-2}(1 + x^2[2p - 1])}{1 - \kappa_0(1 + x^2)^{p-1}}. \quad (10)$$

Comparing this expression for $0 < \kappa_0 < 1$ to the corresponding expression for $\kappa_0 = 1$, one can show that the latter is always greater or equal to the former, for any value of x , and p . Therefore the maximum value of the image distortion in subcritical lenses of Equation 1 can be obtained from Equation 10 with $\kappa_0 = 1$ and small x . This maximum value, $L/W = 3$, is independent of μ and p . Thus the single image of any subcritical lens is rather undistorted, regardless of its impact parameter and magnification.

From Figure 2 it appears that supercritical clusters with $\kappa_0 \lesssim 2$ can produce undistorted images with $\mu \gtrsim 10$. We will now show that in a realistic supercritical cluster the probability of detecting undistorted images is negligible. To address this, we need to reintroduce the projected source position, y . The bottom panel of Figure 1 shows the distortion and image position as a function of source position for images of a $\kappa_0 = 1.1$ lens (solid lines). It may seem that images II and III are undistorted. Image III tends to fall very close to the centre of the cluster, as is seen in the upper panel. Since a core radius, i.e. $x = 1$, typically corresponds to $\sim 50h^{-1}$ kpc, an image at $x \lesssim 0.1$ will probably be hidden within the central cluster galaxy. That leaves us with a small range of impact parameters in the range $\log(y) \sim -2$ to -1.8 which could produce detectable undistorted magnified images of type II. For typical cluster parameters that range translates to roughly 0.1 arcsecond and is thus smaller than a typical source, i.e. a galaxy several kpc across at $z_s \sim 0.5 - 2$. Additionally, as the L/W ratio changes very rapidly at these y 's, an extended image will appear distorted.

[‡] We give our definition of magnified and undistorted later in Section 4.3, but for now we assume that such images have magnification $\gtrsim 10$, and aspect ratio $\lesssim 3$.

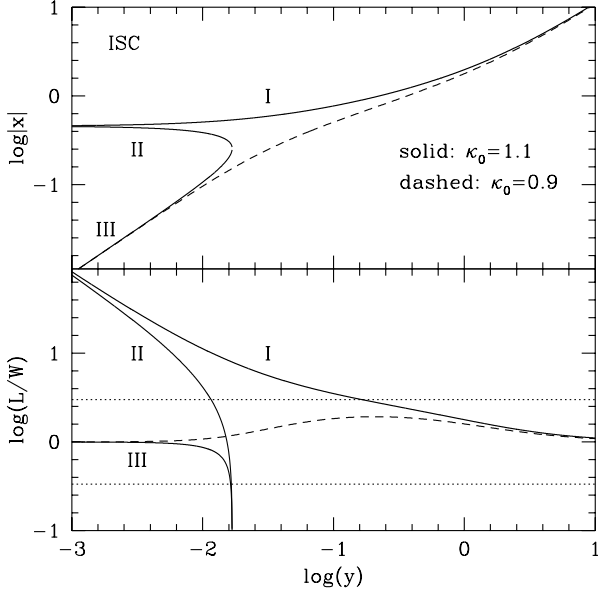


Figure 1. Image position, $|x|$, (top panel) and length-to-width ratio, (bottom panel) vs. source impact parameter, y , for two ISC lenses: $\kappa_0 = 1.1$ (solid lines) and $\kappa_0 = 0.9$ (dashed line) of the ISC cluster model. Roman numerals indicate image type. The dotted lines in the bottom panel bracket the ‘undistorted’ image region, see Section 4.3.

3.2 NFW model

The NFW lens model is singular at the centre for all values of κ_s (Equations 5, 6), and so is formally supercritical. This profile will always produce three images if the source impact parameter is sufficiently small.

Figure 3 shows the relation between the image position, x and source position, y . Note that the values of κ_s were picked such that the total mass within $2.5h^{-1}$ Mpc of these clusters is the same as that of ISC clusters with $\kappa_0=1.1$, and 0.5 (see Section 4.1). The images are labeled as in Figures 1 and 2, and have similar properties to those described in Section 3.1. The major difference when compared to the ISC model is that there is no NFW case that would correspond to a subcritical, i.e. single-image-only ISC cluster. In fact, relations between image properties, y vs. x (Figure 3), and L/W vs. μ (Figure 4), are qualitatively the same regardless of the value of κ_s . In particular, the distortion of the primary images of all NFW clusters is an increasing function of magnification; therefore giant arcs would be a common type of image in these clusters.

Clusters with $\kappa_s \gtrsim 0.3$ cannot have magnified undistorted images at all (Figure 4), but those with smaller values of κ_s have parts of all three image branches in the HMU region. Since we are interested in HMUs let us derive equations describing image properties for small κ_s cases. We will take advantage of the fact that for small κ_s models the triple image region moves towards small x , see top panel of Figure 3. Equation (2.10) of Bartelmann (1996) gives function $g(x)$, which is proportional to the mass interior to x ; $m(x) = 4\kappa_s g(x)$. For small x , this simplifies to

$$g(x) \approx -\left(\frac{x}{2}\right)^2 (2 \ln[\frac{x}{2}] + 1), \quad (11)$$

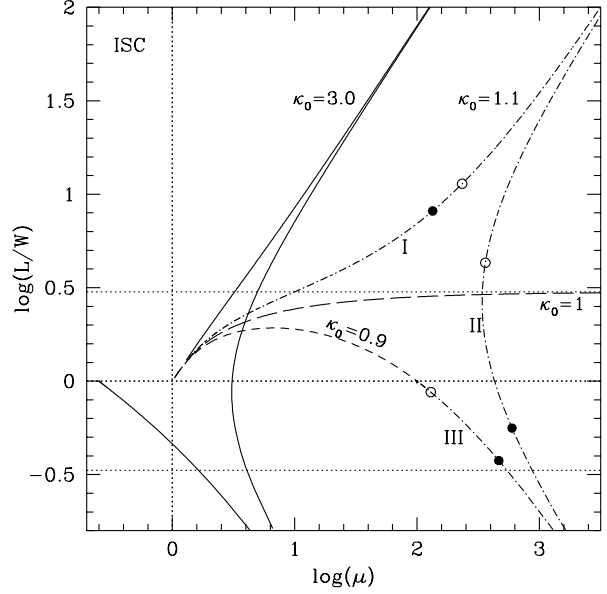


Figure 2. Magnification vs. distortion of images formed by an isothermal cluster with a core, ISC, represented by Equation 1. Supercritical clusters ($\kappa_0 = 3.0$, solid lines; $\kappa_0 = 1.1$, dot-dash lines) have three image branches each. Just-critical ($\kappa_0 = 1.0$, long-dash line), and subcritical ($\kappa_0 = 0.9$, short-dash line) clusters always have one image. The images are labeled as in Figure 1. Horizontal dotted lines at $L/W = 3$ and $\frac{1}{3}$ mark the region of undistorted images. The three empty (solid) circles are images of a source at $y = 0.010$ ($y = 0.016$). Notice that for the primary images of supercritical lenses, $\log(\mu)$ is proportional to $\log(L/W)$. Just subcritical lenses, on the other hand, produce images of high magnification and small distortion.

and the lens equation 7 becomes,

$$y \approx x(1 + 2\kappa_s \ln[\frac{x}{2}] + \kappa_s). \quad (12)$$

The condition for radial critical curve is $dy/dx = 0$, which can be solved for the radius of the corresponding radial caustic in the source plane,

$$y_r \approx -4\kappa_s e^{-(3/2+1/[2\kappa_s])}. \quad (13)$$

This equation shows that no matter how small κ_s , y_r will remain finite, and therefore all NFW clusters can produce 3 images.

The corresponding expressions for magnification and length-to-width of the images are derived from Equations 7, 5, 6, and 2, assuming small x :

$$\mu \approx \left| (1 + 3\kappa_s + 2\kappa_s \ln[\frac{x}{2}]) (1 + \kappa_s + 2\kappa_s \ln[\frac{x}{2}]) \right|^{-1} \quad (14)$$

$$L/W \approx \left| \frac{(1 + 3\kappa_s + 2\kappa_s \ln[\frac{x}{2}])}{(1 + \kappa_s + 2\kappa_s \ln[\frac{x}{2}])} \right| \quad (15)$$

These demonstrate that a line of constant L/W in Figure 4 intersects the primary image branches of various κ_s models at magnifications such that $\mu \propto \kappa_s^{-2}$. Therefore as one goes to less massive clusters the magnification of primary images of a given fixed distortion increases. Therefore highly magnified undistorted images of infinitesimally small sources are possible with low-mass NFW clusters.

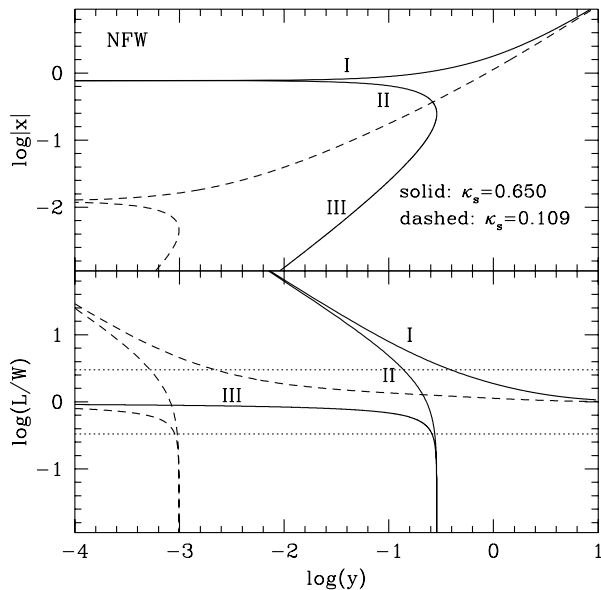


Figure 3. Image position, $|x|$, (top panel) and length-to-width ratio (bottom panel) vs. source impact parameter, y , for two lenses: $\kappa_s = 0.650$ (solid lines) and $\kappa_s = 0.109$ (dashed line) of the NFW cluster model. Roman numerals indicate image type.

To determine if these images will stay undistorted for sources of finite size, one needs to look at how L/W changes with y , i.e. the bottom panel of Figure 3. For $\kappa_s = 0.109$ images II and III arise only for sources at $y \lesssim 0.001$. For typical r_s of $300h^{-1}$ kpc, this corresponds to ~ 0.1 arcsecond, which is smaller than the expected source size. Therefore images of type II and III would not produce HMUs. The primary image shows more promise; the region of $\mu \gtrsim 10$ in Figure 4 corresponds to source position range $y \sim \text{few } 0.001\text{--}0.01$, or ~ 1 arcsecond.

4 MODEL ASSUMPTIONS

In the last Section we have shown that both ISC and NFW models can produce HMUs under certain conditions. Next, we need to estimate the relative frequency of occurrence of HMUs with the two cluster models. Assuming that the cluster and the sources are at fixed redshifts, this involves two steps: first, for a given cluster one has to integrate over source impact parameters, taking into account finite source size, and second, integrate over the distribution of clusters properties.

4.1 Galaxy clusters

We assume that galaxy clusters form a one-parameter family, with the core radius r_c of ISC and scale radius r_s of NFW being fixed, but possessing a range of masses. The cluster mass function, $dN(M)/dM$, is derived from two observed relations of X-ray selected clusters. Based on a sample of EMSS clusters, Henry et al. (1992) derive cluster luminosity function to be, $dN/dL_X \propto L_X^{-\alpha_X}$, where α_X varies with redshift but is approximately 0.3 between the redshifts of 0.15 and 0.6. A relation between cluster bolometric luminosity,

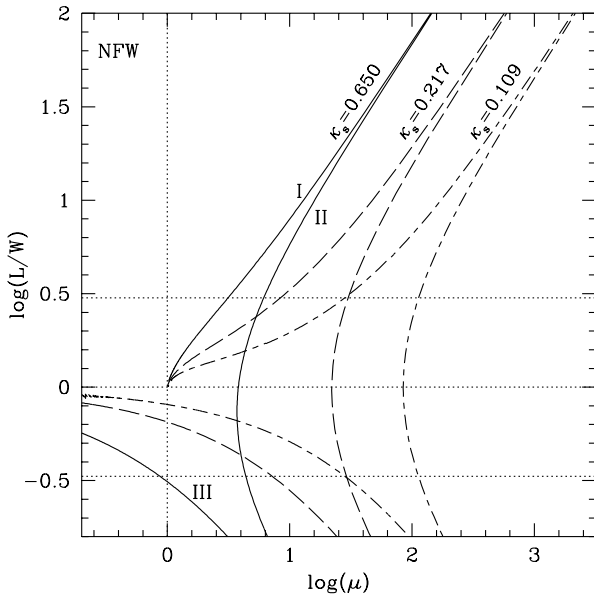


Figure 4. Magnification vs. distortion of images formed by an NFW cluster model, represented by Equations 5, 6. All clusters, regardless of κ_s have three images each if source impact parameter is sufficiently small. The images are labeled as in Figure 3. Horizontal dotted lines at $L/W = 3$ and $\frac{1}{3}$ mark the region of undistorted images. The three values of κ_s represented in this Figure, 0.650, 0.217, and 0.109, were picked such that these clusters have the same mass inside $2.5h^{-1}$ Mpc as the ISC ones with $\kappa_0 = 3.0, 1.0$, and 0.5 , respectively.

derived from EXOSAT data, and velocity dispersion is given by Edge & Stewart (1991): $L_X \propto \sigma_v^{-2.9}$. Combining these two relations with the assumption that $M \propto \sigma_v^2$, we arrive at cluster mass function,

$$dN(M)/dM \propto M^{-3.9}. \quad (16)$$

The absolute normalization is irrelevant, since we will only be dealing with ratios. We need not assume an upper or lower cluster mass limits: the lower mass cutoff is effectively achieved because low mass clusters have a negligible lensing cross-section, while at the upper mass end the lensing cross-section increases slower than the rate at which the numbers of clusters decrease due to the steep slope of their mass function.

We fix the core radius r_c at $50h^{-1}$ kpc, which is substantially smaller than the derived X-ray ‘core’ sizes, but is consistent with lensing observations (Fort & Mellier 1994). For the NFW clusters, we fix r_s at $300h^{-1}$ kpc, which is close to a typical value obtained in the Navarro et al. (1996) simulations.

With the physical length scale of the two cluster models fixed, we can now derive the correspondence between the one-parameter ISC and NFW models, i.e. we ask what is the relation between κ_0 and κ_s of clusters that have the same mass within $2.5h^{-1}$ Mpc. The latter is roughly equal to r_{200} , and corresponds to $50r_c$ and $8.33r_s$, respectively. Using Equations 4, 5 and 6 we obtain $\kappa_0 \approx 4.615\kappa_s$.

4.2 Sources

We assume that the unlensed parent population of HMUs is the same as that of arcs in clusters. The half-light radii of the sources of arc images are almost the same as the observed widths of the arcs, because the cluster potential is not expected to distort tangential arc images in the radial direction. Smail et al. (1996) measure half-light radii for a sample of 8 HST arcs (see their Figure 5). The average half-light radius is about 0.5 arcseconds, which is what we will adopt in the present paper. We further assume that all the sources are circular with a uniform surface brightness.

At any given redshift the luminosity function (LF) of sources is assumed to be a power law, with the slope corresponding to that of the Schechter LF, α . The value of α is estimated to be about 1.1 locally, but may have been steeper in the past, $\alpha \sim 1.5$ (Ellis et al. 1995). We use both values below, to account for the possible range of α 's depending on the type of galaxies and their evolution. The results are not very sensitive to α . We neglect the sources brighter than L_\star , the characteristic luminosity of Schechter LF, because of their small numbers.

We need not make any further assumptions about the source luminosity function, as we explain below. The number of images of type i , where i can be HMU or arcs, for a given cluster characterized by κ_0 or κ_s (or cluster mass M), is given by,

$$n_i \propto \int y \, dy \int_{L_\star}^{L_{lim}/\mu(y)} \left(\frac{L}{L_\star}\right)^{-\alpha} dL \cdot H_i \quad (17)$$

where H_i is the Heviside step function which is 1 if the image selection criteria are satisfied (Section 4.3), and 0 otherwise; L_{lim} is the faintest observable luminosity. The outer integral is over the source impact parameter, y in the source plane. The integral can be written as

$$n_i \propto \int y \left[\left(\frac{L_{lim}}{\mu(y)L_\star}\right)^{1-\alpha} - 1 \right] dy \cdot H_i \\ \approx \left(\frac{L_{lim}}{L_\star}\right)^{1-\alpha} \int y [\mu(y)]^{\alpha-1} dy \cdot H_i, \quad (18)$$

The function $\mu(y)$ is determined by the ISC or NFW model. The last step in the above equation is justified because the minimum magnification μ required for a detectable image is large (Section 4.3), and α is always >1 . Both L_{lim} and L_\star are functions of source redshift, but since we are only interested in the ratio of n_{HMU} to n_{Arcs} , the dependency on these quantities cancels out.

As the results are quite insensitive to z_s we make no assumptions about the source redshift distribution.

4.3 Image selection criteria

Images are selected based on their size or morphology. To be selected as either a giant arc or a HMU, an image has to be lensed appreciably. For an arc to be detected, its L/W has to exceed 10, a commonly used criterium for giant luminous arcs. A HMU is defined as an image with central $\mu > 10$, and $L/W < 3$. Additionally, the undistorted nature of the image is guaranteed by requiring that the change in L/W ratio across the image should not exceed 50%.

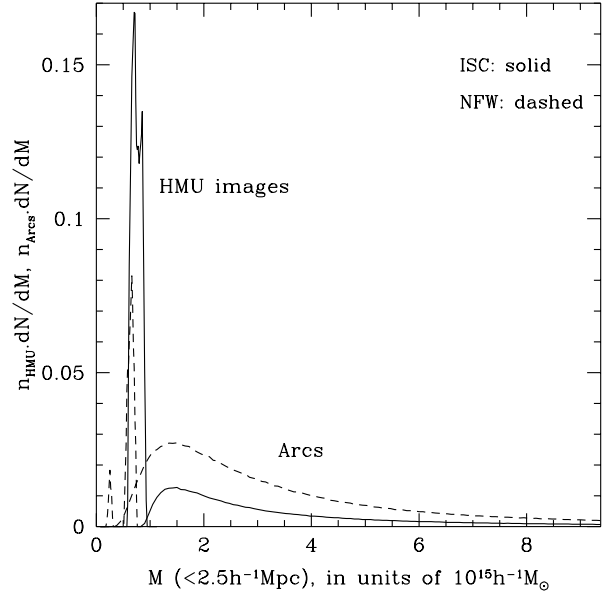


Figure 5. Number of HMU and arc images convolved with the cluster mass function, as a function of cluster mass. The vertical axis has arbitrary normalization. Solid lines are for the ISC model, while dashed lines are for the NFW model. Source and lens redshifts were fixed at $z_s = 0.3$ and $z_l = 1.0$; Schechter LF slope was assumed to be $\alpha = 1.5$.

	z_s		
z_l	0.5	1.0	2.5
0.2	1.28 (1.53)	1.22 (1.46)	1.21 (1.44)
0.3	1.27 (1.55)	1.16 (1.40)	1.14 (1.37)
0.4	1.42 (1.78)	1.13 (1.36)	1.08 (1.31)

Table 1. The ratio of the number of HMU images to arcs in the ISC model, i.e. f_{ISC} , for a range of source, z_s and lens, z_l redshifts. Two values of the Schechter LF slope α were tried: 1.5, and 1.1 (in parenthesis).

5 RESULTS

Figure 5 shows the numbers of giant arcs and HMUs per cluster, weighted by the cluster mass function. The numbers plotted along the vertical axis are proportional to $n_i \cdot dN(M)/dM$, where n_i is given by Equation 18, and $dN(M)/dM$ by Equation 16. The solid and dashed lines represent ISC and NFW models, respectively, and arcs and HMUs are labeled. Here we assumed $z_l = 0.3$, $z_s = 1.0$, and

	z_s		
z_l	0.5	1.0	2.5
0.2	0.35 (0.47)	0.34 (0.44)	0.33 (0.44)
0.3	0.25 (0.34)	0.23 (0.30)	0.19 (0.30)
0.4	0.20 (0.29)	0.16 (0.22)	0.16 (0.21)

Table 2. Same as Table 1, but for the NFW model.

$\alpha = 1.5$. Notice that for both mass profiles, HMU images are produced by low mass clusters only, as was explained in Sections 3.1 and 3.2. The relative numbers of HMU and arc images produced by ISC and NFW profiles can be understood intuitively. The shapes of images depend on the mass density gradient at the location of the images (Section 2). The core region of ISC is flat, hence it produces roughly equal radial and tangential magnifications, and is therefore ideal for generating HMUs. The projected density of the NFW profile, on the other hand, goes as $-\ln\frac{x}{2}+1$ at small x , and so does not have a flat core. It is also steeper than isothermal at large radii. Overall, the NFW profile is steeper than ISC, and thus is better than ISC at making giant arcs, and worse than ISC at making HMUs.

We are interested in the ratio of HMUs to giant arcs for a given cluster model, i.e.,

$$f_{\text{model}} = \frac{\int n_{\text{HMU}}(M) \cdot [dN(M)/dM] dM}{\int n_{\text{Arcs}}(M) \cdot [dN(M)/dM] dM}, \quad (19)$$

where the model is either ISC or NFW. This is just the ratio of the areas under the HMU and arc curves in Figure 5. For the parameters of the Figure, $f_{\text{ISC}} = 1.16$, and $f_{\text{NFW}} = 0.23$.

Table 1 shows how the f_{ISC} ratio changes with source and lens redshift. The numbers (in parentheses) are for the Schechter LF slope α of 1.5 (1.1). Table 2 contains the corresponding values for the NFW model. It is seen from these two tables that the predictions are virtually independent of source redshift, but depend on lens redshift. The source and lens redshift come in only in Σ_{crit} (Equation 3), and both of these trends arise because of the way Σ_{crit} , which determines cluster's lensing strength, varies with z_l and z_s . When z_l is held constant, Σ_{crit} attains its asymptotic value at redshifts just beyond z_l , and thus source redshift has very little effect on f . On the other hand, when z_s is constant, Σ_{crit} changes quite rapidly at low-moderate lens redshifts. The sense of the trend is also understood in terms of Σ_{crit} : when the lensing strength of a cluster of a certain mass increases due to the decrease in Σ_{crit} , more arcs are produced, and hence f goes down. The weak dependency on z_s is a useful feature because source redshift distribution is arguably the most uncertain of the relevant model parameters.

The f ratios depend somewhat on the source LF slope, α . The dependency is not very strong because most of the images are magnified just by the minimum required μ (because the cluster cross-section declines rapidly with μ), and so both HMUs and arcs are drawn from a rather narrow portion of the LF. The decline in cluster cross-section with μ is more severe for HMUs because of the additional selection restrictions placed on undistorted images. Therefore, when α is steeper and there are more faint sources, the number of HMU images does not increase as much as the number of arcs; hence f is smaller for steeper LFs.

Dependence on cosmology is weak. Tables 1 and 2 assume flat Universe model, dominated by a cosmological constant; $\Omega = 0.2$, $\Lambda = 0.8$. Adopting a matter-dominated flat Universe, $\Omega = 1.0$, produces at most a 40% increase in f . Since f is the ratio of the numbers of images, it does not depend on the Hubble constant.

Note that the predictions for relative numbers of HMUs to giant arcs are a function of chosen image selection criteria. For example, if minimum HMU magnification is increased from 10 to 30, then f_{ISC} drops by about a factor or 10 com-

pared to the tabulated values, but virtually no HMUs are expected with the universal dark matter profile.

6 CONCLUSIONS

In this paper we considered two cluster mass density profiles, isothermal sphere with a core and a universal dark matter profile, and studied the properties of gravitationally lensed images of extended sources produced by these models. We were particularly interested in highly magnified undistorted images, and have shown that both profiles can in principle produce such images, though when realistic cluster properties and mass functions were folded in, ISC models proved to be much more efficient than NFW at making HMU images. Using simplified assumptions, we calculated f , the ratio of HMUs to giant arcs for the two models, as a function of source and lens parameters. To account for cluster asymmetries and substructure, which were not considered in this paper, the derived f ratios should be multiplied by the ratio of the frequency of arcs in substructured clusters to that in smooth symmetric clusters. The latter ratio can be obtained from numerical simulations of the type described in Bartelmann et al. (1995). We have shown that f is not very sensitive to cosmology, source luminosity function and redshift distribution, and lens redshift distribution.

In fact, the strongest dependency by far is on the cluster model: with the ISC model HMUs are on average 1.2 times as abundant as giant arcs, whereas with the NFW model HMUs are only 0.2 times as common as arcs (see Tables 1 and 2). *Thus relative frequency of highly magnified undistorted images to giant arcs can be used to discriminate between isothermal clusters with cores and universal dark matter halo profiles*, if a complete sample of clusters is examined for HMU/arc images. Two points need to be stressed here. First, since HMUs are produced by clusters at the lower end of the mass function, $M(< 2.5h^{-1}\text{Mpc}) \lesssim 10^{15}h^{-1} M_{\odot}$, a cluster sample should extend down to such masses, or corresponding X-ray luminosities; alternatively, model predictions should make an allowance for a high-mass cluster cutoff. Second, HMUs would not be as easily detected as giant arcs, since they would have regular morphology. If they are at high redshift their surface brightness will be correspondingly low. However, they should be appreciably larger than typical high- z galaxies, with half-light radii of about 1.5–2 arcseconds. To find HMUs one would need to do spectroscopy on extended, low surface brightness galaxies with regular morphology, located within 10–20 arcseconds of cluster centres, in clusters with no giant arcs. Extensive searches with such observational constraints have not been undertaken; therefore it is not surprising that highly magnified undistorted images, whether their number density on the sky is comparable to or much smaller than that of giant arcs, have so far escaped detection.

ACKNOWLEDGMENTS

We would like to thank Alastair Edge, Richard Ellis, and Mike Irwin for helpful suggestions regarding an early version of the paper. LLRW would like to acknowledge the support

of PPARC Fellowship at the Institute of Astronomy, Cambridge, UK.

REFERENCES

- Bartelmann, M., Steinmetz, M. & Weiss, A. 1995, *Astron. and Astrophys.*, **297**, 1.
- Bartelmann, M., 1996, Preprint, available as astro-ph/9602053.
- Blandford, R. D. and Narayan, R., 1986, *Astrophys. J.*, **310**, 568.
- Colley, W. N., Tyson, J. A., Turner, E. L., 1996, *Astrophys. J.*, **461**, L83.
- Ebbels, T. M. D., Le Borgne, J.-F., Pello, R., Ellis, R. S., Kneib, J.-P., Smail, I. and Sanahuja, B., 1996, *Mon. Not. R. astr. Soc.*, **281**, L75.
- Ellis, R. S., Colless, M., Broadhurst, T., Heyl, J., and Glazebrook, K., 1995, *Mon. Not. R. astr. Soc.*, **280**, 235.
- Edge, A. C. and Stewart, G. C., 1991, *Mon. Not. R. astr. Soc.*, **252**, 428.
- Fort, B. and Mellier, Y., 1994, *Astr. Astrophys. Rev.*, **5**, 239.
- Hammer, F., 1991, *Astrophys. J.*, **383**, 66.
- Henry, J. P., Gioia, I. M., Maccacaro, T., Morris, S. L., Stocke, J. T., and Wolter, A., 1992, *Astrophys. J.*, **386**, 409.
- Kneib, J.-P., Mellier, Y., Pello, R., Miralda-Escudé, J., LeBorge, J.-P., Böhringer, H. and Picat, J.-P., 1995, *Astron. and Astrophys.*, **303**, 27.
- Lavery, R. J. 1996, *Astron. J.*, **112**, 1812.
- Lavery, R. J., and Henry, J. P., 1988, *Astrophys. J.*, **329**, L21.
- LeFèvre, O., Hammer, F., Angonin, M. C., Gioia, I. M. and Lupino, G. A., 1994, *Astrophys. J.*, **422**, L5.
- Miralda-Escudé, J., and Babul, A., 1995, *Astrophys. J.*, **449**, 18.
- Navarro, J. F., Frenk, C. S. and White, S. D. M., 1996, *Astrophys. J.*, **462**, 563.
- Navarro, J. F., Frenk, C. S. and White, S. D. M., 1995, *Mon. Not. R. astr. Soc.*, **275**, 720.
- Sadat, R., 1997, *Preprint*, also available as astro-ph/9702050.
- Schindler, S. et al. 1995, *Astron. and Astrophys.*, **299**, L9.
- Schneider, P., 1985, *Astron. and Astrophys.*, **143**, 413.
- Schneider, P., Ehlers J. and Falco E. E. , 1992, *Gravitational Lenses*, Springer-Verlag Press.
- Seitz, S., Saglia, R. P., Bender, R., Hopp, U., Belloni & Ziegler, B. 1997, *Preprint*, also available as astro-ph/9706023
- Smail, I., Dressler, A., Kneib, J.-P., Ellis, R. S., Couch, W. J, Sharples, R. M., Oemler, A., 1996, *Astrophys. J.*, **469**, 508.
- Waxman, E. and Miralda-Escudé, J., 1995, *Astrophys. J.*, **451**, 451.
- Williams, L. L. R. and Lewis, G. F., 1996, *Mon. Not. Roy. Ast. Soc.*, **281**, L35.
- Wu, X.-P. and Hammer, F., 1993, *Mon. Not. Roy. Ast. Soc.*, **262**, 187.
- Yee, H. K. C., Ellingson, E., Bechtold, J., Carlberg, R. G. and Cuillandre, J. C., 1996, *Astron. J.*, **111**, 1783.